ACS Biomaterials SCIENCE & ENGINEERING
Cite This: ACS Biomater. Sci. Eng. XXXX, XXX, XXX−XXX
Article
pubs.acs.org/journal/abseba

Improvement of Tribological and Biocompatibility Properties of Orthopedic Materials Using Piezoelectric Direct Discharge Plasma Surface Modification

Ardalan Chaichi,[†] Alisha Prasad,[†,∥] Lijesh Kootta Parambil,[†,∥] Shahensha Shaik,[†] Ali Hemmasian Ettefagh,[†] Vinod Dasa,[‡] Shengmin Guo,[†] Michelle L. Osborn,[§] Ram Devireddy,[†] Michael M. Khonsari,[†] and Manas Ranjan Gartia*[,†]

[†]Department of Mechanical and Industrial Engineering, Louisiana State University, Baton Rouge 70803, United States
[‡]Department of Orthopaedic Surgery, Louisiana State University Health Sciences Center, New Orleans 70112, United States
[§]Department of Comparative Biomedical Sciences, School of Veterinary Medicine, Louisiana State University, Baton Rouge 70803, United States

Supporting Information

ABSTRACT: Various types of alloys and polymers are utilized in orthopedic implants. However, there are still several issues accompanied by the use of prosthetic materials, such as low wear performance and catastrophic failure. Surface enhancement of biomaterials is a promising method that can improve the success rate of prosthetic operations without negatively affecting their bulk properties while improving the biocompatibility of implants and reducing infections. Nonthermal plasma treatment has become a ubiquitous surface modification method in sterilization and healthcare applications. However, the clinical applications of such an approach have been limited due to the lack of detailed studies delineating the wear behavior and biocompatibility of implants after plasma treatment. In this study, we have employed a handheld piezoelectric direct discharge (PDD) plasma generator to modify the surface of two common metallic (Ti6Al4V) and nonmetallic (GUR1020 polymer) biomaterials used typically in joint and disc replacements. We have observed an approximately 60-fold reduction in tribological wear rate along with a 2- to 3-fold increase in the biocompatibility properties of plasma coated samples compared to noncoated (untreated) surfaces, respectively. Our study introduces a novel application of nonthermal PDD plasma technology that is capable of increasing the quality and success rate of joint and disc replacements.

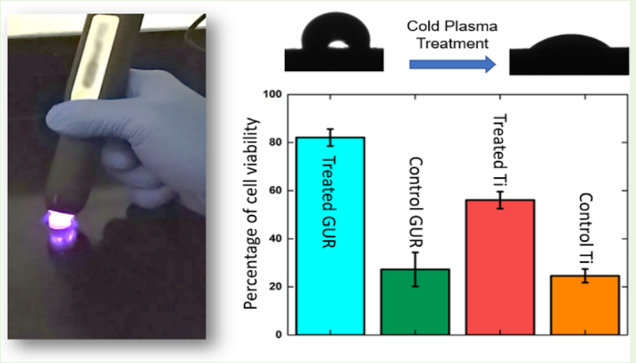

KEYWORDS: *surface modification of biomaterials, joint and disc replacement, nonthermal plasma, Ti6Al4V, GUR1020 UHMWPE*

1. INTRODUCTION

Joint and disc replacement via the knee and hip are growing considerably due to the increasingly aging population as well as the higher demand for an active lifestyle in the elderly population.[1−3] However, the longevity of implants is significantly limited by wear performance, corrosion, biocompatibility, and postsurgery infection.[4−6] These factors are correlated to each other, and effectively addressing any of them can dramatically improve the quality of prosthetic performance and lifespan. To this end, presurgical measures should be taken to maximize the performance of joint and disc implants.[7] Thermal stabilization and electron beam and γ irradiation are the most conventional approaches employed for the enhancement and engineering of biomaterials.[8,9] However, these methods are accompanied by drawbacks such as degradation of bulk properties (toughness, fatigue, and tensile strength) but do improve the surface features and characteristics.[10] This degradation in bulk properties could cause catastrophic failure in some implants under high cyclical loads or extreme loading conditions, such as knee prosthesis.[2] Additionally, more recent techniques like Ar plasma modification require thermal stabilization that tends to negatively affect bulk properties.[11] Furthermore, the conventional plasma coating methods are not cost efficient and require extremely large machinery, rendering them inappropriate for clinical applications. During the past decade, nonthermal plasma has been widely investigated mostly because of the associated antimicrobial effects and surface sterilization capabilities.[12,13] However, most studies on this subject have been performed on polymeric materials while the tribological behavior of nonthermal plasma treated surfaces has

Received: January 2, 2019
Accepted: April 15, 2019
Published: April 15, 2019

DOI: 10.1021/acsbiomaterials.9b00009
ACS Biomater. Sci. Eng. XXXX, XXX, XXX−XXX

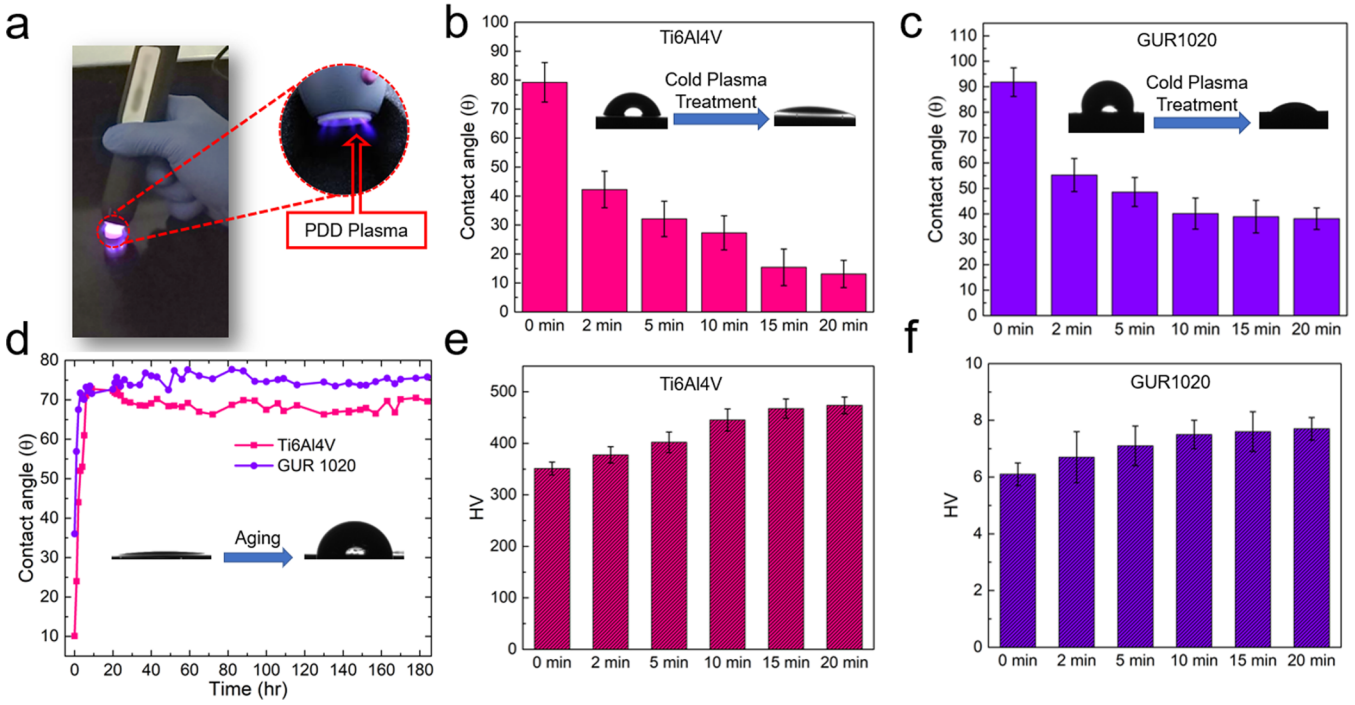

Figure 1. Contact angle and microhardness measurements of treated and untreated samples for six different time intervals. (a) Illustration of GUR1020 pellet surface treatment by means of handheld PDD plasma generator. (b) Water contact angle decreases by increasing the plasma exposure time for Ti6Al4V. (c) Plasma treatment improves the hydrophilicity of GUR1020 sample. (d) Aging experiment shows the formation of a temporary and a permanent coating due to plasma exposure. (e) The value of microhardness increases by increasing the exposure time for Ti6Al4V. (f) Microhardness of the GUR1020 sample increases due to plasma exposure. Each test was repeated at least 10 times, and each exposure experiment was performed on a separate sample.

remained uninvestigated. Piezoelectric direct discharge (PDD) plasma is categorized as a novel nonthermal plasma generating method in which the cold plasma is produced due to a direct discharge in a piezoelectric transformer.[14] In this method, a compact handheld device (Figure 1a) can be used to produce cold plasma (<50 °C) without the requirement of external gas cylinders. Similar devices are suitable for healthcare and clinical applications due to the safety and ease of operation. Yet there are still no published studies that thoroughly examine the potential surface enhancements of PDD for prosthetic applications.

Ti6Al4V is an extensively employed material in a highly corrosion resistant and biocompatible $\alpha-\beta$ titanium alloy with a high strength-to-weight ratio.[15−17] However, poor wear properties of this alloy under cyclic loadings restrict its effectiveness as an implant in high load-bearing areas like in the knee and hip.[18−20] As a result, researchers are working on a wide variety of surface enhancements and coatings to mitigate this issue. Gallardo-Moreno et al.[21] have shown that the formation of titanium oxide on the surface of Ti6Al4V improves the physicochemical properties of this alloy for biomedical applications. Accordingly, creation of a thin oxide layer on Ti6Al4V can significantly improve its biocompatibility as well as the wear resistance properties.

GUR1020, on the other hand, is an ultrahigh molecular weight polyethylene (UHMWPE) used in prosthetic applications due to its high biocompatibility, high toughness, and ease of fabrication methods.[22−24] These properties degrade over cyclic loading conditions because of poor wear resistance.[25,26] Therefore, the lifespan of GUR1020 implants is limited to less than 10 years after surgery.[27] Subsequently, the implant needs to be replaced with a new one to prevent infection and potential pain caused by the worn-out debris of the prosthesis. Hence, several coating methods (such as γ irradiation, ion irradiation, and plasma surface modification) have been proposed to extend the longevity of GUR1020 implants by improving the tribological properties.[28−30] However, these methods are impractical at the clinical level due to the complexity and size of machinery, safety issues, and detrimental effects on bulk properties of the prosthesis.

In this study, we have investigated the potential surface modification of Ti6Al4V and GUR1020 by means of a handheld PDD plasma generator to scrutinize surface changes through the treatment process and their effect on tribological, corrosion, and biological properties. This study explores new horizons for clinical applications of nonthermal plasma research and pioneers the introduction of a practical surface treatment method that can be utilized prior to prosthetic surgeries in a clinical setting.

2. MATERIALS AND METHODS

2.1. Materials. High strength grade-5 Ti6Al4V (ASTM B348) rods (diameter 1.3 cm) were purchased from McMaster-Carr (Douglasville, GA). The rods were then machined into smaller pellets with a thickness of 3 mm for further characterization and biocompatibility experiments. Titanium pins were also machined from the same rod to be used in tribological tests. Medical grade GUR1020 UHMWPE compression molded rods with diameter of 5 cm were purchased from Total Plastics Int'l Life Sciences (Fort Wayne, IN). The chemical structure of GUR1020 is shown in Figure S1. GUR1020 is a linear polyethylene with very good aberration and mechanical properties due to considerably higher density (937 kg/m^3) and molecular weight (3.5 × 10^6 g/mol) compared to standard polyethylene (due to longer polymer chain length). GUR1020 is produced from powder by means of compression molding and extrusion processing methods. GUR1020 is one of the very common materials in orthopedic implants mainly due to its special mechanical and biocompatibility properties. Pellets and

DOI: 10.1021/acsbiomaterials.9b00009
ACS Biomater. Sci. Eng. XXXX, XXX, XXX−XXX

discs were machined from the GUR1020 rod for further characterization and tribological and biological tests, as detailed below.

2.2. PDD Plasma Generator. The Relyon Plasma Piezobrush PZ2 (12 V dc, 30 W) handheld device was purchased from Relyon Plasma GmbH (Regensburg, Germany) and used for surface plasma treatment of samples. Although the device is capable of using external gas cylinders (like Ar, He, O_2, etc.), we investigated the used of ambient air to facilitate the easy transition to a clinical setting. The ambient air was fed into the PDD device via a feeding fan on back of the device. The temperature of generated plasma was always less than 50 °C, and all the treatments were performed at room temperature with a relative humidity of 30−50%. The distance between the plasma generator and surface was kept constant at 5 ± 1 mm. All the experiments were performed on treated samples right after the plasma exposure without any delays.

2.3. Characterization Tests. A Krüss (Hamburg, Germany) drop shape analyzer was utilized for contact angle measurements and wettability studies. Distilled water (2 μL) was used to measure the contact angle between surface and liquid. For aging experiments, the water contact angle of the 20 min plasma treated samples was measured at different time points for both GUR1020 and Ti6Al4V materials. Microhardness measurements were performed by a Ratnakar Vickers hardness tester with a tetragonal pyramid diamond tip (vertex angle of 136°) under the loading of 100 g and holding time of 30 s. A Thermo Nicolet Nexus 670 ATR-FTIR equipped with a DTGS detector, a Globar source, a Smart iTR diamond ATR accessory, and a Renishaw inVia confocal Raman microscope (laser: 532 nm) was used to analyze the characteristics of GUR1020 before and after plasma exposure. A Scienta Omicron ESCA 2SR X-ray photoelectron spectroscope (XPS) with the monochromatic Al Kα X-ray source (1486.7 eV) was utilized for surface analysis of Ti6Al4V and GUR1020. An ion gun (Ar gas) with beam energy of 3 keV, emission current of 3.8 μA, filament current of 10 μA, and angle of 45° was used for surface etching. The Stopping and Range of Ions in Matter (SRIM) software package was employed to estimate the ion etching depth in the matter; the same parameters of the experimental setup were applied to simulations. A PANalytical Empyrean multipurpose diffractometer was utilized to perform X-ray diffraction (XRD) experiments ($\lambda_{X\text{-}ray}$ = 0.154 nm) in the 2θ range 10−90°.

2.4. Tribological Tests. To understand the variation in the tribological performance of GUR1020 and Ti6Al4V with the plasma treatment, a pin-on-disc setup (Figure S2) was utilized. In this experiment, the Ti6Al4V pin was stationary, and it slid over the rotating GUR1020 disc in the presence of phosphate-buffered saline (PBS). The pin and disc were fixed to the pin and disc holders, respectively. The experimental setup is shown in Figure S2. To simulate the walking motion, the disc was subjected to an oscillatory motion of 24° angle at an oscillatory speed of 60 rpm and a load of 30 N (1 MPa pressure). In this work, we have used nine different conditions (0:0, 10:0, 20:0, 0:10, 10:10, 20:10, 0:20, 10:20, and 20:20) for surface treatment of the samples (five samples for each condition) to investigate the effect of different exposure times on the tribological behavior of this system (polymeric disc and metallic pin). The first number for each experiment indicates the exposure time (min) of the plasma for the GUR1020 disc, and the second number indicates the exposure time (min) of the plasma for the Ti6Al4V pin. All experiments were performed at the same radius of contact. To check the repeatability, experiments were performed 5 times. Nine different specimens were developed by treating both pin and disc with plasma for 0, 10, 20 min. The specimens were evaluated by measuring (i) wear volume rate from the measured wear depth values and (ii) friction coefficient values. Wear volume (w_v) can be determined by[31,32]

$$w_v = \pi R^2 \delta \quad (1)$$

where R is the radius of pin (m) and δ is the wear depth (m). The surface roughness of the specimen was measured using a 3D profilometer [Bruker (model 831-775) with a 5× objective].

2.5. Corrosion Tests. Three-electrode cell corrosion experiments were performed by employing a CHI-604C instrument equipped with a reference electrode (saturated calomel electrode (SCE)), counter electrode (platinum electrode), and Ti6Al4V sample as the working electrode, which was molded by cold epoxy. The exposed areas of all samples to the electrolyte media were ∼1 cm^2. Phosphate-buffered saline (PBS) was chosen as the solution with naturally dissolved oxygen at 37 °C. Tafel curves were plotted in the voltage range −1 to 2 V vs saturated calomel electrode (SCE) (1.67 mV/s). Samples were polished with sand papers (grit size 320-1000) prior to the tests. The variation of corrosion potential with time was measured immediately after the immersion of the samples for 20 min.

2.6. Cell Study. *2.6.1. Cell Culture (Adipose-Derived Stem Cells (ASCs) to Osteogenic Stem Cells (OSCs) Differentiation).* ASCs obtained from subcutaneous adipose tissue were purchased and cryopreserved for cell culture. A frozen batch of ASCs was suspended in stromal growth medium StromaQual (LaCell LLC, LA, USA) containing a mixture of 10% DMSO and 90% FBS. The cells were thawed in a 37 °C water bath until the sample liquefied. The ASCs were then suspended in a growth medium with serum and cultured until passage 1. Here, passage 1 refers to the time point when the resuspended cryopreserved cells have reached 90% confluency. The cells collected from passage 1 were cultured in a 12-well plate at a density of 1 × 10^4 cells/cm^2. The cell culture was performed in an incubator at 37 °C, 5% CO_2 for 24−36 h and checked until confluency. After reaching 90% confluency, the cells were inoculated only on one side of the surface of the polymer and titanium discs. The cells on the surfaces were cultured for 21 days in an osteogenic medium (OsteoQual purchased from LaCell LLC, LA). The culture media were replaced every 3 days. The controls were suspended in stromal medium. The schematic representation of the osteogenic stem cell study timeline is provided in Figure S3.

2.6.2. Cell Viability. The cell viability was determined on the basis of the live/dead cell assay by staining the cells with fluorescent dyes Calcein AM/propidium iodide with final concentrations at 2 and 3 μM, respectively. A fluorescence microscope (Zeiss SteREO Lumar.V12) with an excitation/emission filter at 550/565 nm was utilized to count the number of live−dead cells (shown as green−red color in the images).

2.6.3. Immunohistochemistry. Cells were characterized after fixation with 4% paraformaldehyde for 30 min followed by permeabilization with 0.2% TritonX-100 in PBS for 5 min. Blocking was performed for 45 min at 4 °C with 0.2% fish skin gelatin (FSG) on the fixed and permeabilized samples for the immunofluorescence experiments. Dyes that were used for the immunofluorescence imaging were phalloidin, CF488A (Biotium, USA), RUNX 2 mouse antibody sc-390351 AF594 (Abcam, USA), and osteocalcin mouse antibody sc-74495 AF594 (Abcam, USA). On days 7 and 14, phalloidin and RUNX 2 stains were used to characterize the cytoskeleton and preosteoblasts. On day 21, cells were stained with phalloidin and osteocalcin to characterize the cytoskeleton and mature osteoblasts. All cells were counterstained with 2 μg/mL of 200 μL Hoechst (Thermo Fisher Scientific, USA) in PBS for 1−2 min to identify the nucleus. Images were captured at 10× magnification using confocal microscopy (Leica TCS SP8 confocal microscope with WLL) at $\lambda_{460/490}$ for Hoechst, $\lambda_{488/510}$ for phalloidin, and $\lambda_{594/650}$ for RUNX2 and osteocalcin, respectively. Alizarin red S (Sigma-Aldrich, USA) staining was also conducted to identify calcium containing cells on day 21 differentiated cells. Images were captured at 10× magnification using a bright field microscope.

2.6.4. Gene Expression. The osteogenic gene expression was evaluated by RNA isolation, followed by a quantitative reverse transcription-polymerase chain reaction (RT-PCR) experiment to identify RUNX2, osteopontin, and osteonectin on days 14 and 21, respectively. A Purelink RNA kit (Life Technologies, CA, USA) was utilized for the isolation of RNAs from the stem cells. A nanodrop spectrophotometer was used to check the quality of the extracted RNAs and quantify their amount. cDNA synthesis was performed using a commercial kit (Applied Biosciences, CA, USA). For the qPCR quantification, SYBR green dye (Applied Biosystems, CA) was used in an RT-PCR system (ABI-7900). The osteogenic gene primer sequences were obtained from Li et al.[33] The primer sequence for GAPDH gene (housekeeping gene) was obtained from our previous work.[34] The gene

DOI: 10.1021/acsbiomaterials.9b00009
ACS Biomater. Sci. Eng. XXXX, XXX, XXX−XXX

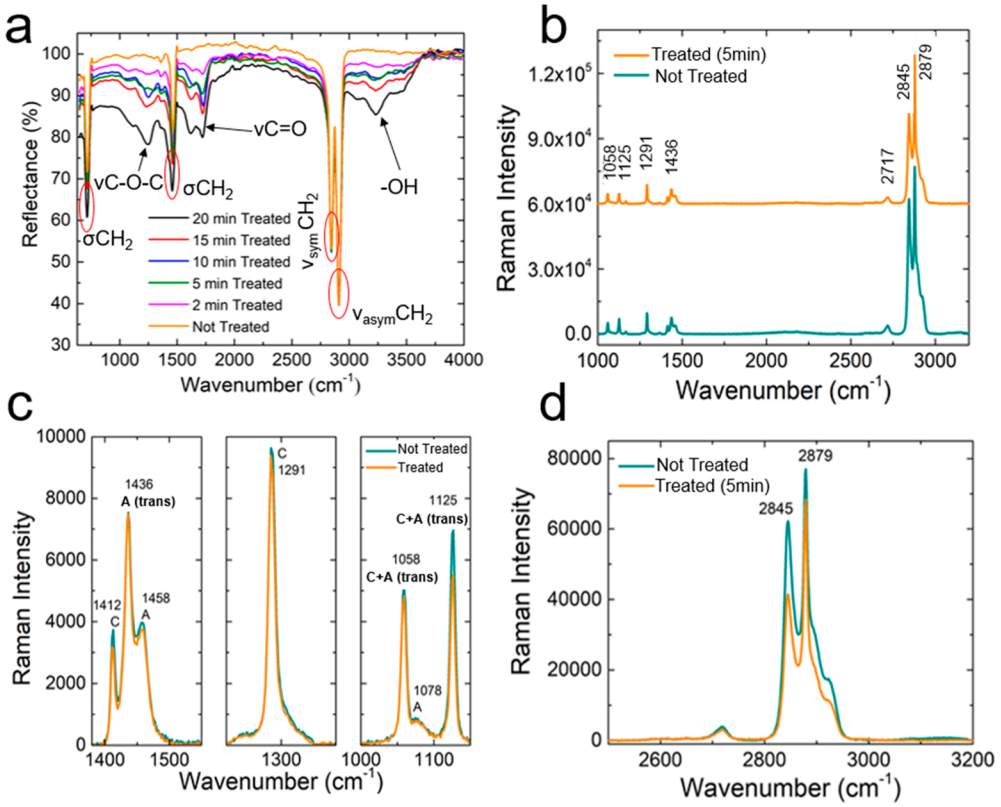

Figure 2. Vibrational spectroscopy of treated and untreated GUR1020. (a) FTIR spectra of GUR1020 after different exposure times show the formation of new chemical groups. (b) Raman spectrum of treated and untreated polymer in the range 1000−3250 cm^{-1} with a 532 nm laser shows the typical peaks of GUR1020. (c) Analysis of Raman spectrum in fingerprint region for treated and untreated polymer shows the variation of peak intensity due to plasma exposure. (d) Analysis of Raman spectrum in the high wavenumber region for the polymer sample shows an increase in crystallinity of the treated sample.

expression was normalized to GAPDH to find the fold-changes and was calculated by the $2^{-(\Delta\Delta Ct)}$ method.[35]

X-ray computed tomography (μCT) images of the implants were obtained with a SCANCO Medical AG (Switzerland) model μCT 40 system using a voltage of 55 kVp, a current of 145 μA, and a voxel size of 10 μm. Scanning was conducted to check the spreading of cells on the implants at 1 °C/min using a SKYSCAN 1074 portable X-ray microtomograph (Bruker, NJ, USA). The 3D images were constructed using Avizo 5.0 software. Cells were fixed with 4% paraformaldehyde and stained with 0.01% osmium tetroxide for 24 h, followed by washing three times with PBS before scanning.

3. RESULTS AND DISCUSSION

3.1. Characterization. Figure 1a shows the plasma handheld device in action coating a GUR1020 pellet. Figure 1b,c demonstrates the contact angle measurement results of Ti6Al4V and GUR1020. Plasma treatment of the surface reduced the water contact angle from 79.2° to 13.1° for Ti6Al4V and from 91.8° to 38.1° for GUR1020 samples. Accordingly, both metal and polymer proved to become considerably hydrophilic due to plasma exposure (~6× reduction in contact angle for metallic sample and ~2.5× reduction in contact angle for polymer sample). Furthermore, the contact angle becomes almost constant after 20 min of plasma exposure which indicates the treatment saturation point for metal and polymer. The lifespan of the coating was measured by conducting the aging experiment (Figure 1d). As a result, two stages were observed during the "aging process". The first stage illustrates the existence of a temporary coating that degrades after about 10 h of aging. The second stage shows a permanent coating that does not degrade over time. Therefore, all the experiments, including biocompatibility tests, were performed right after the plasma exposure without any further delays. Figure 1e,f shows the microhardness measurements conducted on Ti6Al4V and GUR1020 ($p < 0.01$). Accordingly, microhardness of Ti6Al4V and GUR1020 increased by approximately 35% and 26%, respectively, compared to untreated surfaces. Likewise, the saturation point was observed after 20 min of plasma treatment.

The increment in hydrophilicity and microhardness values can be justified by the results obtained from FTIR and Raman spectroscopy analyses. Figure 2a illustrates the ATR-FTIR results of a GUR1020 sample. Different vibrational modes and bonding groups are assigned in Figure 2a to show the changes that occurred during the surface modification at different time intervals. Typical GUR1020 bands can be observed at 713 cm^{-1} (σCH_2; σ = scissoring mode), 1456 cm^{-1} (σCH_2), 2844 cm^{-1} ($\nu_{sym}CH_2$; ν = stretching mode), and 3233 cm^{-1} ($\nu_{asym}CH_2$). The signal intensities of σCH_2 groups have changed slightly due to the plasma treatment. However, there is no considerable intensity change for $\nu_{sym}CH_2$ and $\nu_{asym}CH_2$ groups. On the other hand, the remarkable increase in intensity of νC−O−C (1244 cm^{-1}) and νC═O (1722 cm^{-1}) bands is evidence of the plasma effect on the surface of the polymer. Moreover, the number of −OH (3230 cm^{-1}) species dramatically increased on the surface as a result of plasma treatment. Figure 2b−d shows the Raman spectra of GUR1020 before and after treatment. Typical GUR1020 bands are observed at 1058 cm^{-1} (ν_{asym}C−C), 1125 cm^{-1} (ν_{asym}C−C), 1291 cm^{-1} (τCH_2; τ = twisting mode), 1436 cm^{-1} (σCH_2), 2845 cm^{-1} (ν_{sym} CH_2), and 2879 cm^{-1}

DOI: 10.1021/acsbiomaterials.9b00009
ACS Biomater. Sci. Eng. XXXX, XXX, XXX−XXX

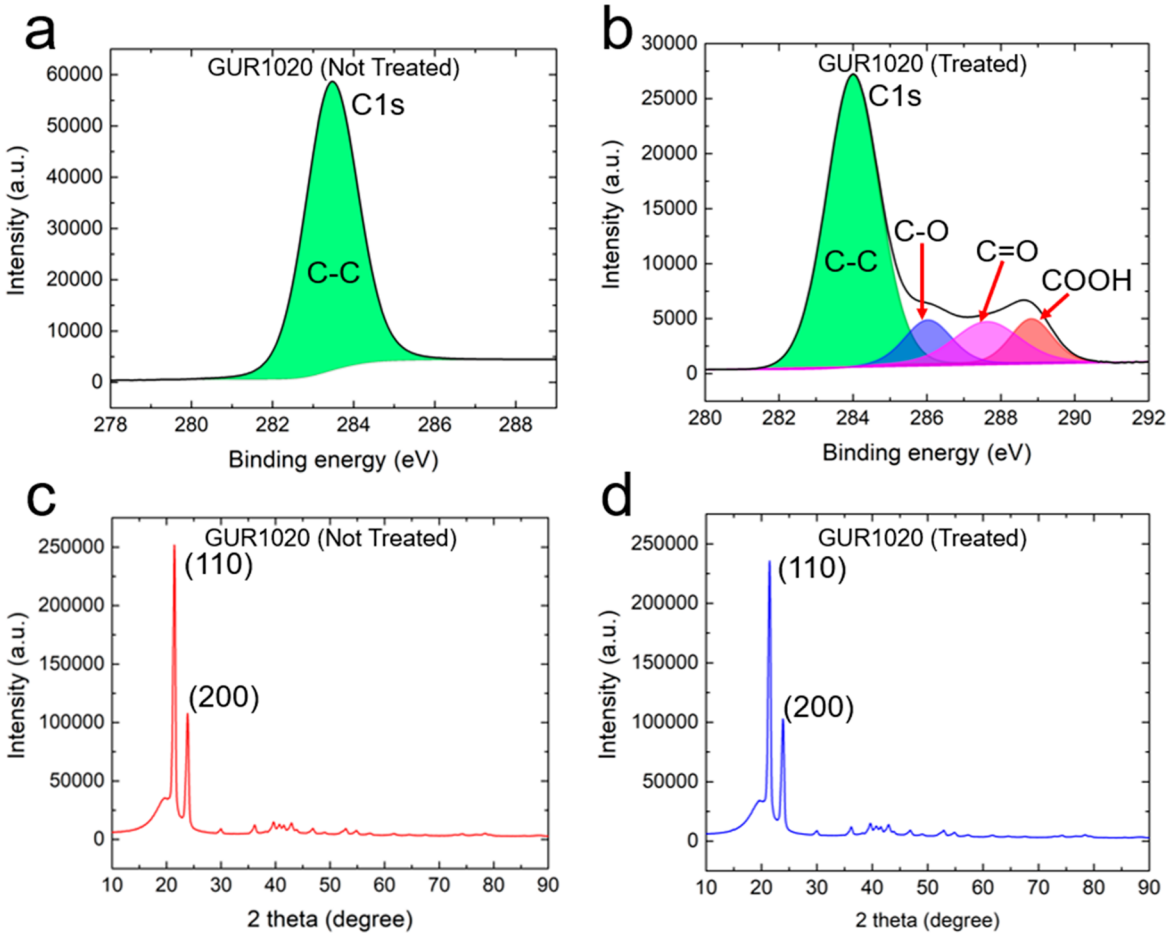

Figure 3. XPS (a, b) and XRD (c, d) analyses of the polymer sample. (a, b) XPS results confirm the formation of new chemical groups after plasma exposure. (c, d) XRD results show that the bulk properties are constant before and after plasma exposure.

($\nu_{asym}CH_2$). From the width and intensity changes of 2845 and 2879 cm^{-1} bands, it can be concluded that the crystallinity of the polymer has increased after the surface modification. Accordingly, the formation of reactive oxygen species and crystallinity improvement are two fundamental reasons for the enhancement of hydrophilicity and hardness on the polymer surface.

To accurately monitor the surface evolution of the samples, XPS studies were conducted for Ti6Al4V and GUR1020. Figure 3a,b shows the deconvoluted C 1s XPS spectrum. Accordingly, the C−C peak was observed at 284 eV for GUR1020 before and after the treatment. Meanwhile, C−O, C═O, and COOH peaks also appeared at 286, 287.6, and 288 eV after performing the surface treatment. On the other hand, XRD analysis was performed to demonstrate that the bulk properties of samples have not been changed due to the surface modification. From Figure 3c,d, (110) and (200) crystal planes of GUR1020 appeared at 2θ values of 21.5° and 23.8°, respectively, for both treated and untreated samples. In addition, interplane spacing (d_{hkl}) was measured by means of eq 2 (Bragg's equation).

$$d_{hkl} = \frac{n\lambda}{2 \sin \theta} \quad (2)$$

Here, n, λ (0.154 nm), and θ are defined as level of diffraction, X-ray wavelength, and Bragg angle, respectively. The interplane spacings for both treated and untreated samples were 0.41 Å (for (110) plane) and 0.37 Å (for (200) plane). Accordingly, XRD spectra of GUR1020 did not change after the treatment. Therefore, it can be concluded that the bulk properties are constant, and this method of plasma surface treatment only changes the surface properties of the polymer.

XPS spectra of Ti 2p in treated and untreated Ti6Al4V are shown in Figure 4a,b. As can be seen, Ti $2p_{3/2}$ and Ti $2p_{1/2}$ peaks are located at 453 and 459 eV, respectively. After the plasma treatment, O_2 species formed on the surface and the TiO_2 $2p_{3/2}$ and TiO_2 $2p_{1/2}$ peaks shifted to 458 and 464 eV, respectively. Moreover, the distance between $2p_{3/2}$ and $2p_{1/2}$ peaks has changed from 6 eV in untreated sample to 7 eV in the treated sample. The aforementioned evidence demonstrates the formation of titanium oxide on the surface of Ti6Al4V due to surface treatment. However, XRD results (Figure 4c,d) do not show any significant change in the bulk properties of Ti6Al4V before and after the surface treatment. According to Figure 4c,d, the most prominent 2θ peaks for both treated and untreated Ti6Al4V appear at 35.4° and 40.4° which are assigned to (010) and (011) planes, respectively. Moreover, intraplane spacing was also the same (~0.25 Å for (010) and ~0.22 Å for (011) plane) for both types of samples regardless of the surface treatment.

To realize the effective depth of PDD plasma on metal and polymer specimens, time dependent Ar ion etching was employed along with XPS analysis to quantify the depth of penetration. First, Ar etching depth was measured by means of SRIM simulation package (details are elaborated in the Materials and Methods). Figure 5a illustrates the simulation

DOI: 10.1021/acsbiomaterials.9b00009
ACS Biomater. Sci. Eng. XXXX, XXX, XXX−XXX

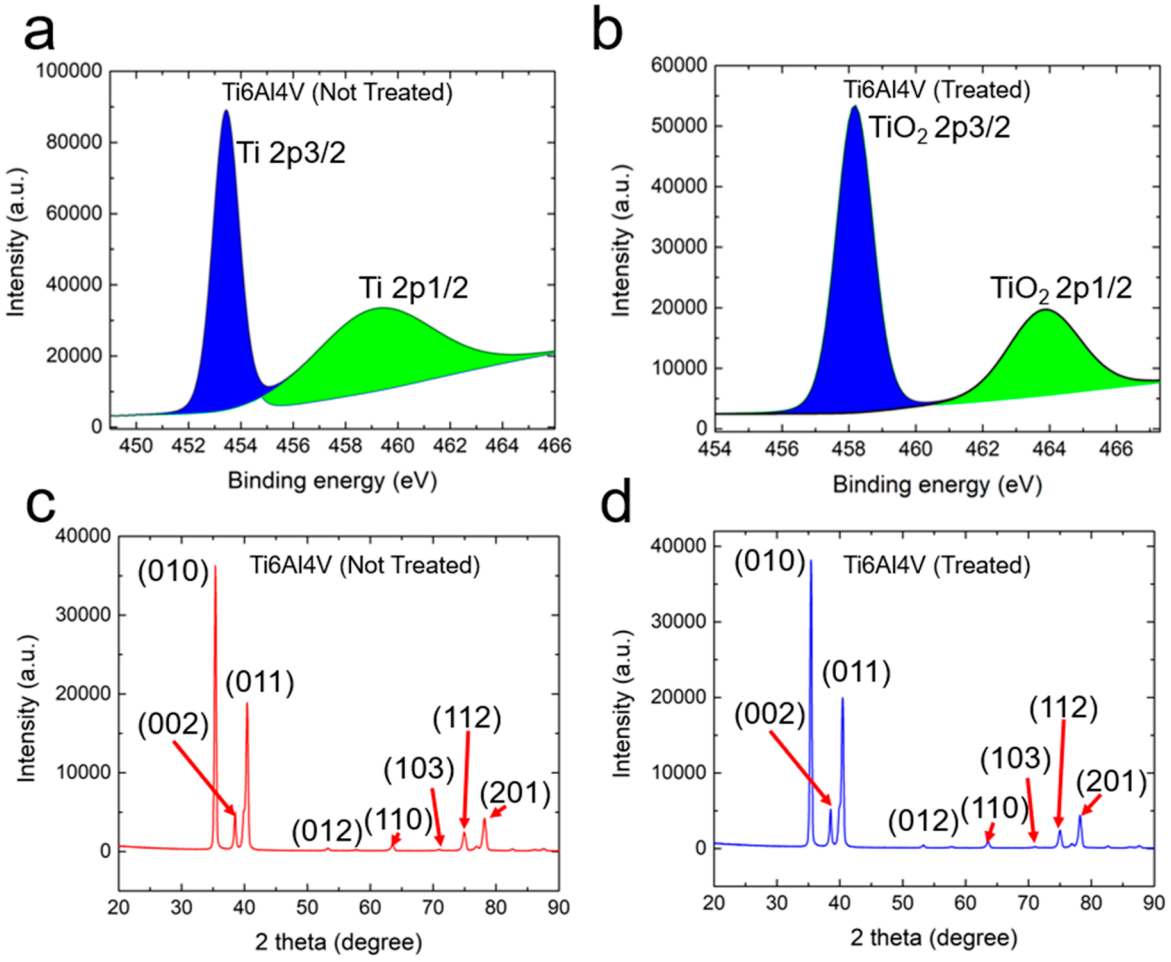

Figure 4. XPS (a, b) and XRD (c, d) analyses of the metallic sample. (a, b) Formation of TiO_2 due to plasma treatment, is illustrated by XPS analysis. (c, d) XRD results confirm that the bulk properties of Ti6Al4V are constant before and after plasma exposure.

results for Ar ion etching of GUR1020 (3D results are provided in Figure S4). Accordingly, the effective depth of etching was measured to be ∼20 nm for every 2 min of etching. Figure 5b shows the O 1s XPS spectrum of the plasma treated sample within 30 min of etching with 2 min intervals. Figure 5b shows the O 1s peak shifting to the left (lower values) from 532.4 to 530.1 eV, and the intensity of peak has decreased as well by increasing the etching time. The decreasing peak intensity shows the decrease in oxygen content. The shift in peak position of O 1s shows that different species of oxygen and the partial species of oxygen are being produced. By comparing the SRIM and XPS results, the effective depth of plasma penetration for GUR1020 was measured to be ∼220 nm (Figure 5c). Furthermore, the same method was performed to calculate the effective depth of plasma treatment for the Ti6Al4V sample (Figure 5d). From Figure 5e, the O 1s peak for Ti6Al4V shifted to the right (higher values) from 529.7 to 531.3 eV and the peak intensity decreased with an increase of etching time. Accordingly, the effective depth of PDD plasma for surface modification of Ti6Al4V was measured to be ∼130 nm (Figure 5f).

3.2. Tribological Behavior. The obtained wear depth data for Ti6Al4V and GUR1020 are plotted in Figure 6a−c for different treatment times. Equation 1 was utilized to calculate the wear volume rate from the wear depth measurement values. The results are shown in Figure 6a−c. Similar to wear depth data, the obtained friction coefficient values are plotted in Figure 6d−f. From Figure 6, it can be observed that transient wear prevailed until the sliding time of 1800 s and that steady state wear was observed afterward. Therefore, in the present work the wear volume rate was calculated for the steady state wear region, and the determined values for different plasma exposure times are plotted in Figure 7a.

To obtain the variation in wear volume rate with plasma treatment, wear volume rate ratio ($w_{untreated}/w_{treated}$) is calculated by dividing the wear volume obtained for untreated samples by wear volume rate for plasma treated samples (with different treatment times). The obtained values are plotted in Figure 7b. From this figure, when both the disc (GUR1020) and pin (Ti6Al4V) are treated for 20 min each, the amount of wear rate was reduced by ∼60× compared to the untreated case. In a comparison of case 20:0 (GUR 20 min; Ti6Al4V 0 min) and case 0:20 (GUR 0 min; Ti64 20 min), it can be concluded that the surface plasma treatment is more effective in reducing wear when the metallic part (Ti6Al4V) is treated with plasma. It is now hypothesized that the reduction in wear with plasma treatment leads to better tribological properties due to the presence of an oxide layer. The presence of an oxide layer on the surfaces of Ti6Al4V and GUR1020 was already discussed in the previous section. As shown in Figure 5c,f, the magnitude of the maximum oxygen percentage (Ti6Al4V, 70%; GUR1020, 28%) and its availability with depth is more than 2.5× in the case of Ti6Al4V compared to GUR1020. Likewise, the oxide layer formation on the surface of the specimen can be indirectly determined by contact angle measurements (Figure 1b−d). The

DOI: 10.1021/acsbiomaterials.9b00009
ACS Biomater. Sci. Eng. XXXX, XXX, XXX−XXX

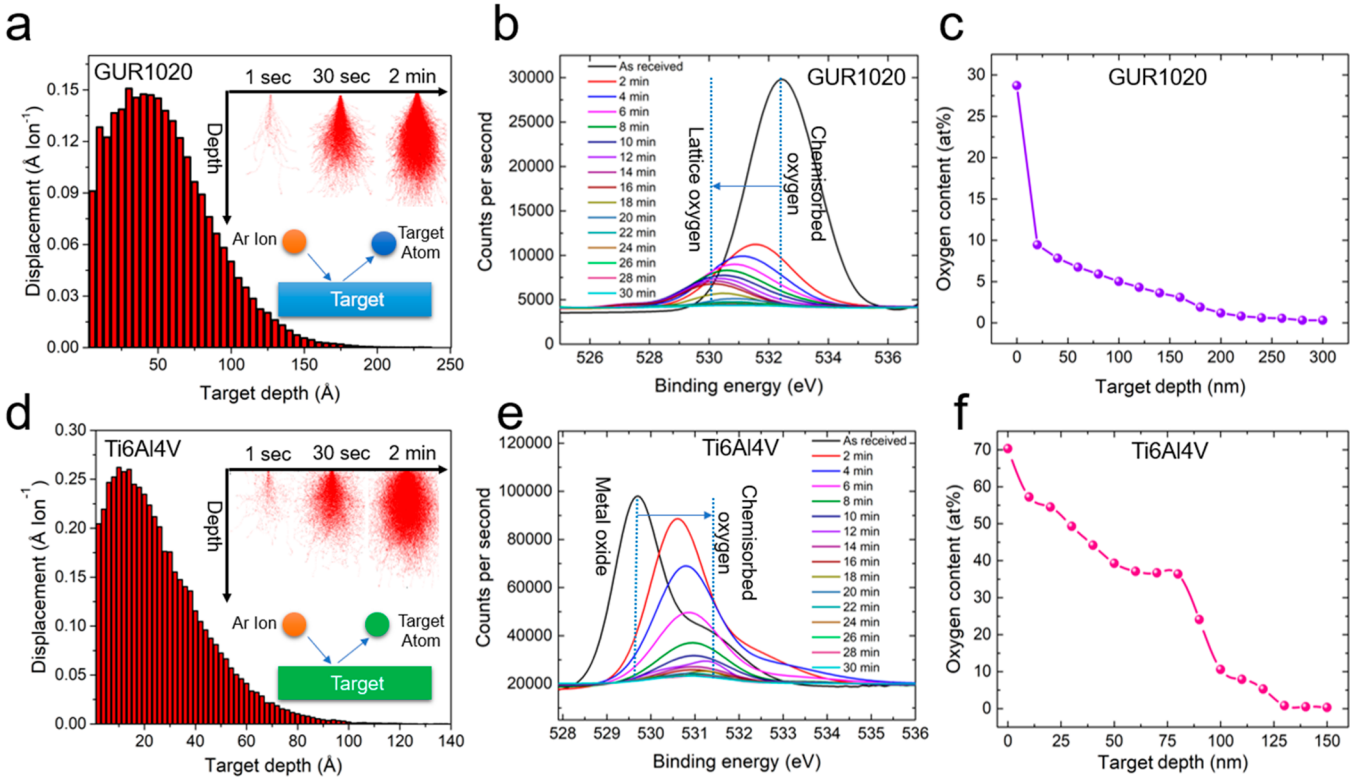

Figure 5. SRIM simulations coupled with experimental XPS results for depth analysis of plasma coating on polymer and metal substrates. (a) SRIM simulation of Ar ion bombardment of the polymer surface. (b) XPS results for the O 1s peak to determine the plasma penetration depth for the polymeric substrate. (c) Oxygen content vs target depth for the polymer sample shows the approximate penetration depth of 220 nm. (d) SRIM simulation of the Ti6Al4V sample bombarded by Ar ions. (e) XPS results for the O 1s peak to determine the plasma penetration depth of the metallic substrate. (f) Oxygen content shows the approximate penetration depth of 130 nm for the Ti6Al4V substrate.

reduction in the contact angles indicates the presence of the oxide layer as well as the change in surface properties (hydrophobic to hydrophilic). This type of surface treatment enhances the wear properties by providing better wettability on the surface. In addition, the increase in microhardness as well as the enhanced wettability improve the tribological properties and reduce the wear volume. Therefore, it can be concluded that the presence of surface oxides, the formation of a hydrophilic layer, and an increase in microhardness result in wear reduction. According to Figure 6d–f, the value of the friction coefficient does not vary considerably by increasing the plasma treatment time on GUR1020. Therefore, it can be concluded that the surface treatment of GUR1020 has a noticeably lower influence on the tribological behavior of the Ti6Al4V–GUR1020 system. Meanwhile, the friction coefficient value decreases dramatically by applying the PDD plasma treatment on the Ti6Al4V surface. As a result, the best tribological properties are achieved when both metallic and polymeric parts are exposed to plasma. Statistical results of the tribological tests are also provided in Figure S5. Accordingly, a good repeatability for tribological tests can be observed.

Figure 7c,d illustrates the surface 3D profile of GUR1020 samples before and after plasma treatment. The average roughness for GUR1020 before and after treatment was measured to be ∼179.8 and ∼181 μm, respectively. Furthermore, the maximum height differences between the peaks and valleys of the surface were ∼3.9 and ∼3.7 μm for untreated and treated samples, respectively. Figure 7e,f shows, for the Ti6Al4V sample, that average roughness was ∼63 nm for the untreated sample and ∼57 nm for the treated sample. Additionally, the maximum peak–valley height difference of samples was ∼203 nm (untreated) and ∼179 nm (treated). Accordingly, the average roughness of samples decreased by ∼5% for GUR1020 and ∼13% for Ti6Al4V. Although the slight decrease in surface roughness might have some effect on the enhancement of tribological properties, this is not a significant factor in this system compared to surface chemistry, wettability, and hardness.

3.3. Corrosion Behavior. Corrosion resistance is a significant factor for biological materials: a poor corrosion resistance increases the risk of implant rejection. It is well-known that Ti and its alloys form a surface oxide layer which improves the corrosion resistance.[36−38] In order to evaluate the corrosion behavior of the samples before and after the surface treatment, open circuit potential (OCP) and Tafel curves were obtained and are presented in Figure 8. On the basis of the OCP curve (Figure 8a), it is clear that, in both samples, the anodic reaction is prevented with the same mechanism while the potential of both samples increased with time. However, the treated sample is more stable thermodynamically. In other words, despite almost the same slope of both curves, the initial potential for the treated sample is more positive, meaning that the surface has become more noble due to the treatment. This may be due to the preformed oxide film on the surface after the surface treatment, as confirmed by characterization experiments in the previous sections.

Tafel curves for untreated and treated samples (Figure 8b) clearly indicate a decrease in corrosion rate and a more noble potential. For the treated sample, the Tafel curve is shifted to the lower values of current density (0.158 μA/cm^2) and more

DOI: 10.1021/acsbiomaterials.9b00009
ACS Biomater. Sci. Eng. XXXX, XXX, XXX−XXX

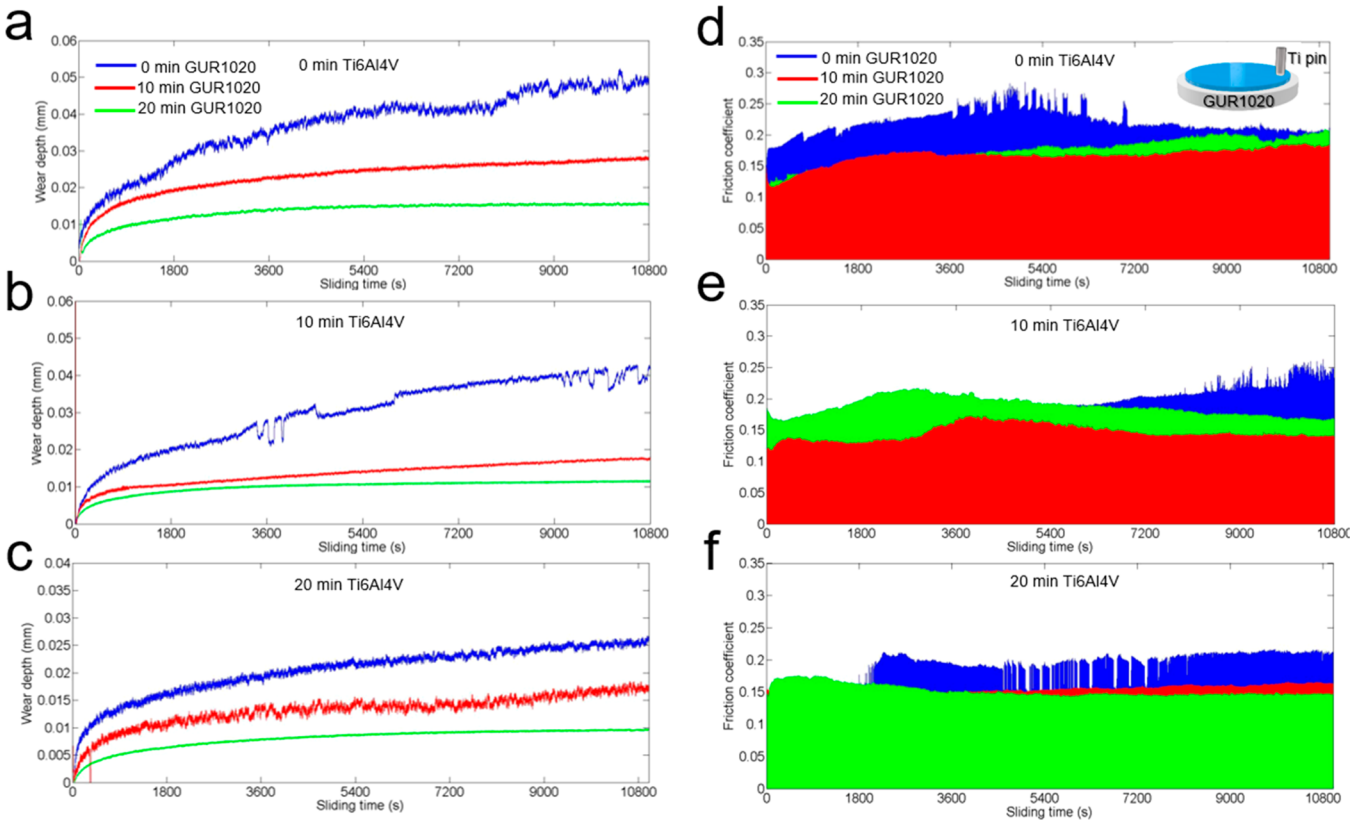

Figure 6. Tribological results for several cases with different plasma exposure times on the metal pin and polymer disc. (a–c) Wear depth vs sliding time for various plasma exposure times shows the improvement of tribological properties by applying the plasma treatment. (d–f) Friction coefficient vs sliding time shows the reduction of friction after plasma treatment of the surfaces.

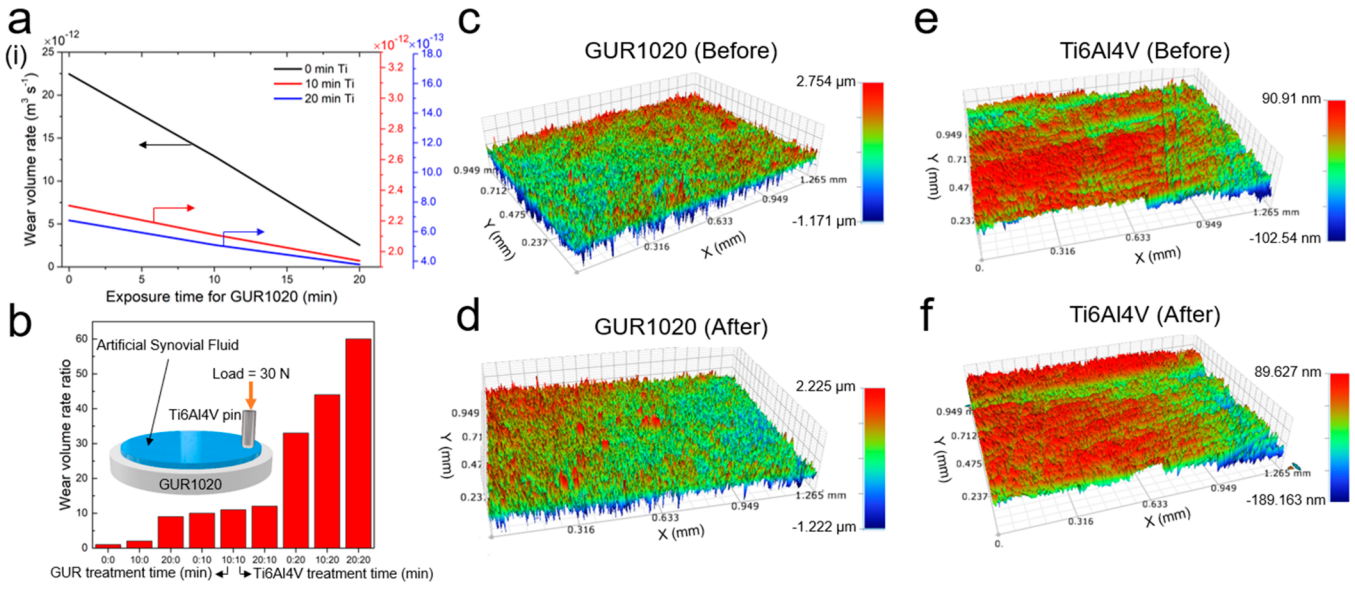

Figure 7. Tribological analysis of polymer and metal substrates before and after plasma treatment. (a) The significant reduction of wear volume due to plasma exposure confirms the improvement of tribological properties. (b) Wear volume ratio for different cases shows the remarkable tribological improvements due to the surface treatment. (c–f) 3D surface profiles of polymer and metal samples show that the roughness of the surface was slightly changed after the plasma exposure.

positive values of potential (−0.402 V). The related measured parameters from the polarization curves are attained by Tafel extrapolation. As mentioned before, the surface treatment forms an oxide layer on the surface, and this layer acts as a protective coating on the surface, thereby maintaining the excellent corrosion resistance of the alloy, and improving it by 37%. As a result, it can be concluded that the nonthermal plasma surface treatment increases the lifetime of the alloy in body fluid and has no negative effect on the corrosion properties of Ti6Al4V.

DOI: 10.1021/acsbiomaterials.9b00009
ACS Biomater. Sci. Eng. XXXX, XXX, XXX−XXX

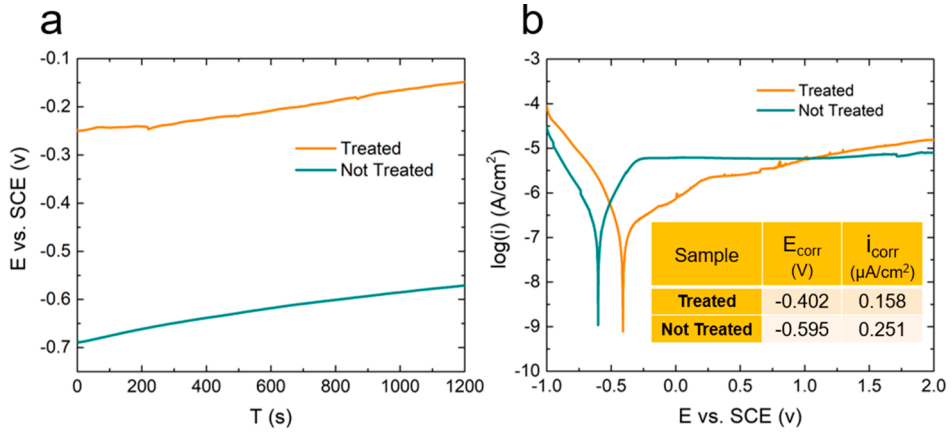

Figure 8. Corrosion behavior of Ti6Al4V before and after surface modification. (a) Potential vs time diagram shows the formation of TiO_2 passive layer after surface modification. (b) Current vs potential diagram illustrates the enhancement of corrosion behavior of the metallic substrate due to surface treatment by shifting i_{Corr} to smaller values.

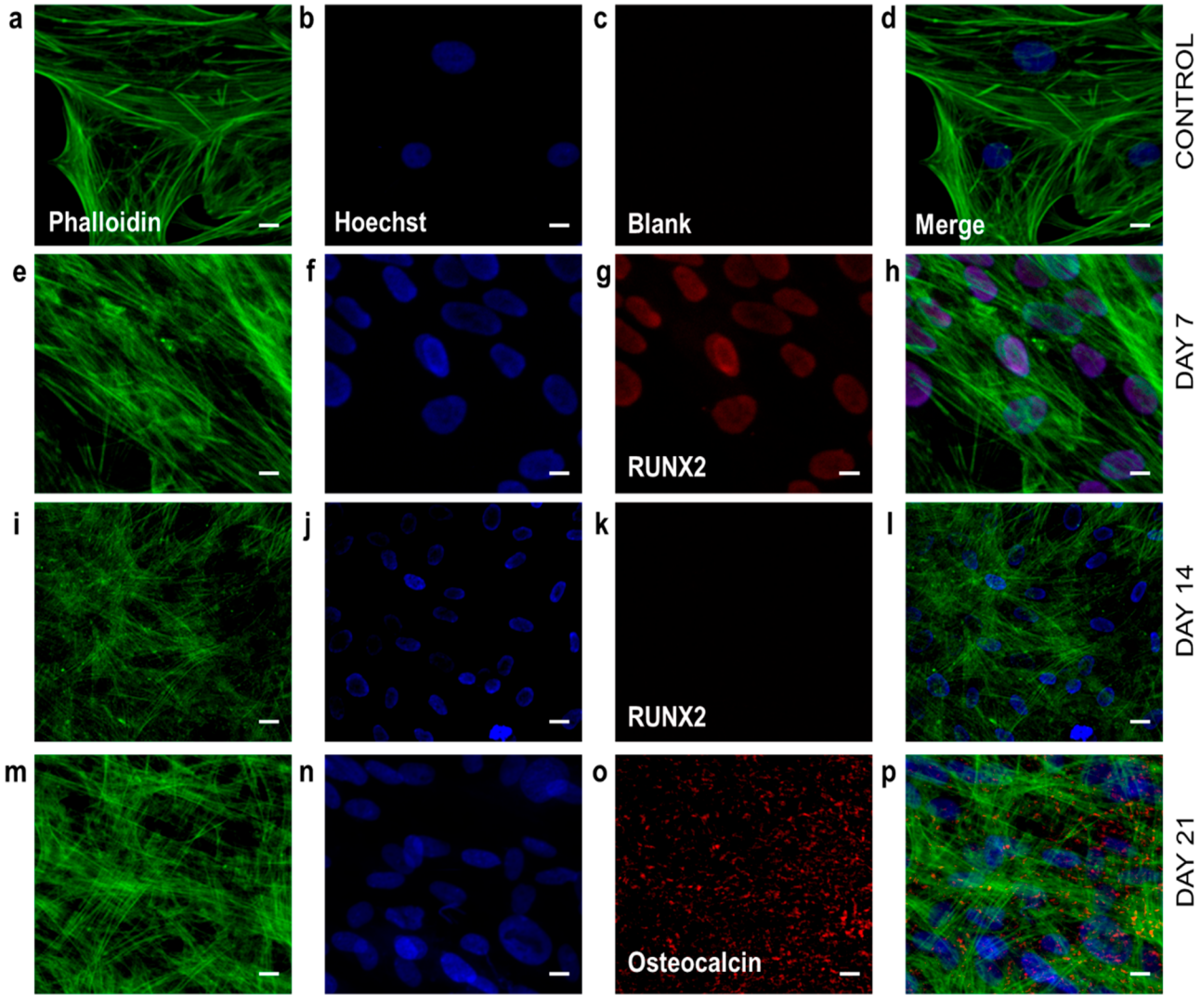

Figure 9. Representative immunofluorescence confocal microscope images of stem cells: column 1 (a, e, i, m) showing phalloidin staining; column 2 (b, f, j, n) showing Hoechst staining; column 3 (individual as labeled); column 4 (d, h, l, p) showing the merged images. (a–d) Control. (e–h) Day 7 osteogenic differentiated stem cells. (i–l) Day 14 osteogenic differentiated stem cells. (m–p) Day 21 osteogenic differentiated stem cells. Scale bar: 1 μm.

Statistical analyses of the corrosion studies are provided in Figure S6, which showed good reproducibility.

3.4. Cell Study. The osteogenic stem cell study timeline as shown in Supporting Information Figure S3 was followed. We

DOI: 10.1021/acsbiomaterials.9b00009
ACS Biomater. Sci. Eng. XXXX, XXX, XXX–XXX

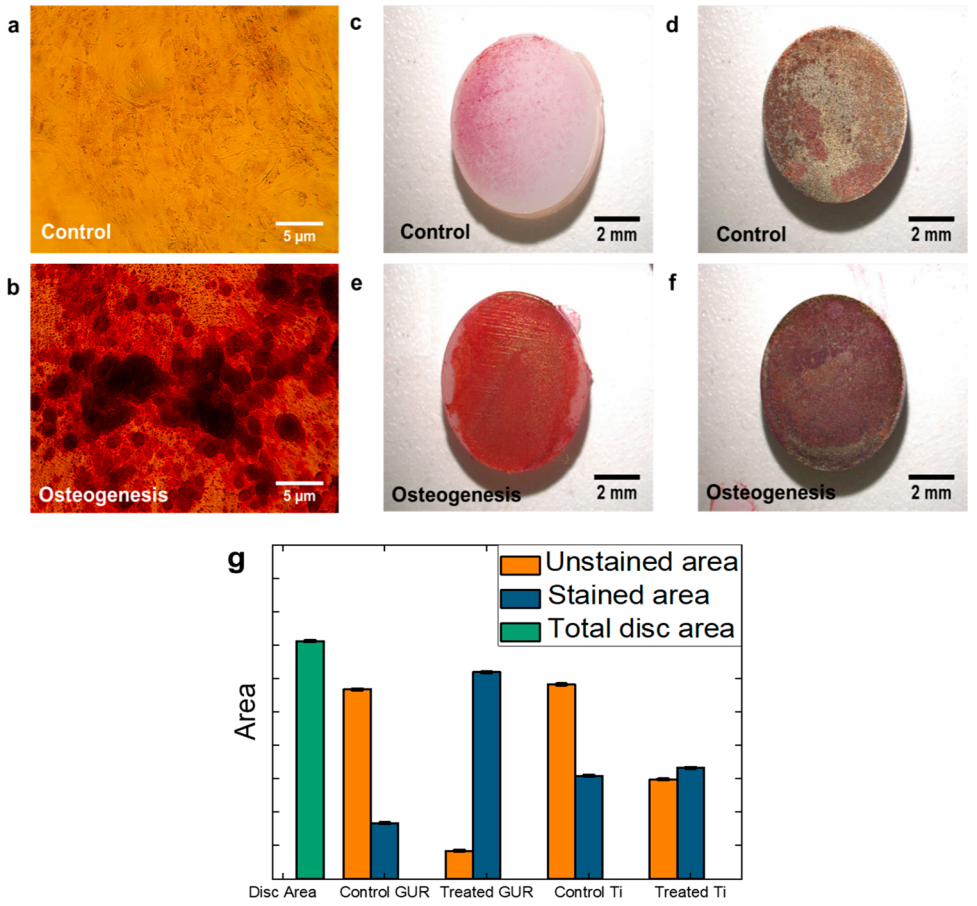

Figure 10. Alizarin red S staining of day 21 stem cells: (a) control and (b) osteogenic differentiated stem cells. Images were acquired at 10× magnification. Scale bar: 5 μm. (c) Control GUR. (d) Control Ti. (e) Treated GUR. (f) Treated Ti. Scale bar: 2 mm. (g) Bar chart showing stained and unstained area for implants (c–f).

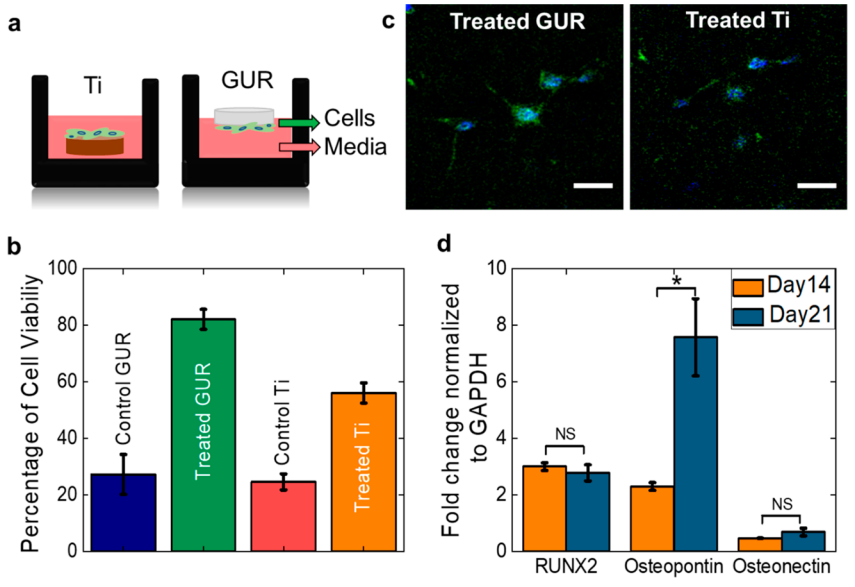

Figure 11. (a) Schematic representation of cell study on the implants. (b) Percentage of cell viability on implants. (c) Representative fluorescence images on treated implants. Scale bar: 0.5 μm. (d) qPCR results of osteogenic genes RUNX2, osteopontin, and osteonectin on days 14 and 21, respectively. * indicates ($p < 0.05$) as statistically significant. NS is not significant ($p > 0.05$).

evaluated the osteogenic stem cell differentiation at three time points: day 7, day 14, and day 21, respectively. Figure 9 shows the fluorescence images of day 7, 14, 21 and their controls, respectively. F-actin filaments were observed on all days with different morphologies. The nucleus colocalization protein RUNX2, and also a preosteoblast marker, was observed on day 7 cells. According to the literature, RUNX2 is likely to occur from day 7 to day 16; however, there might be differences based on

DOI: 10.1021/acsbiomaterials.9b00009
ACS Biomater. Sci. Eng. XXXX, XXX, XXX−XXX

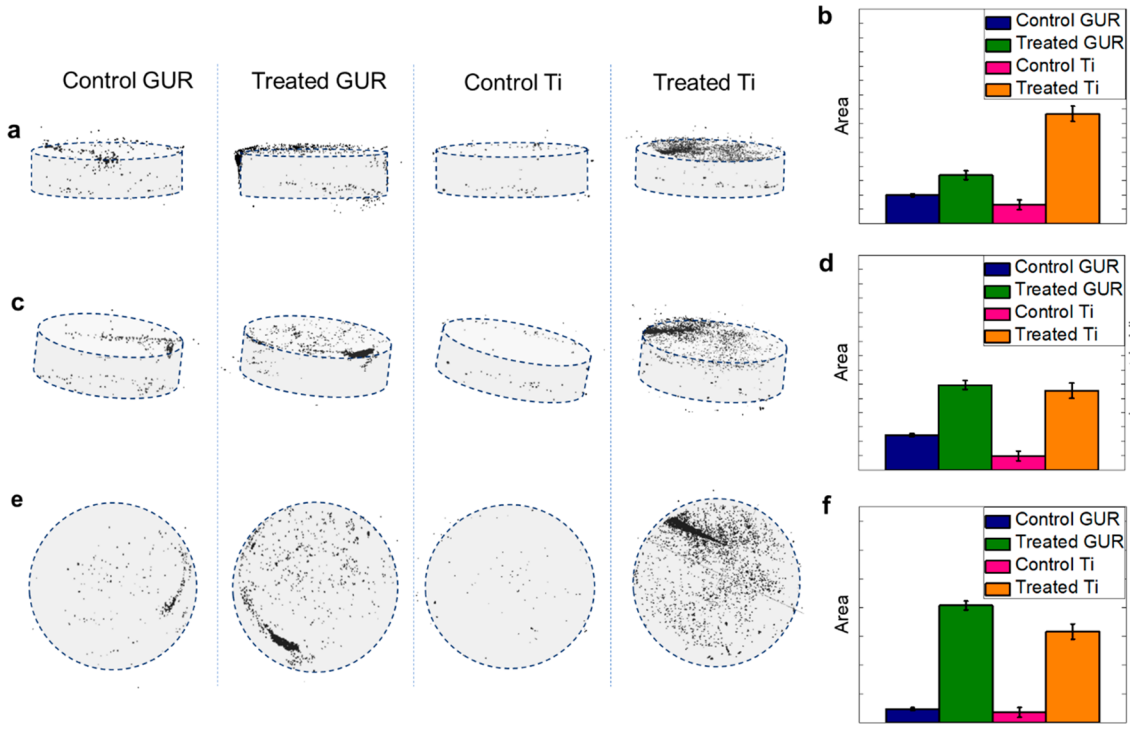

Figure 12. X-ray microcomputed tomography (μCT) images for control and treated implants (GUR and Ti) showing better cell adhesion for treated surfaces. The gray surfaces are the implant samples, and the black dots are the cells. μCT images showing the cells covering the implants in (a) side view, (c) isometric view, and (e) top view for both control and treated surfaces for GUR and Ti samples. The corresponding percentage cell coverage areas are presented in (b) side view, (d) isometric view, and (f) top view.

the age of the donors.[39] The protein osteocalcin, a mature osteoblast marker, was observed on day 21 cells.

Further, we evaluated the calcium containing cells on day 21 differentiated cells by Alizarin red S staining. Figure 10a,b shows the representative images of osteogenic stem cells and controls acquired using a bright field microscope at 10× magnification. We also evaluated the osteogenic potential on the treated implants and their respective controls as shown in Figure 10c–f. The respective areas of Alizarin red stained and unstained area distribution were calculated using ImageJ and are shown in Figure 10g. The quantitative analyses from acquired images were done by image segmenting and thresholding using ImageJ software. Supporting Information Figure S7 shows the demonstration of ImageJ analysis to measure the region of interest (ROI) in histological samples. From the results, it was found that the treated polymer and titanium has a greater amount of calcium deposits in comparison to the nontreated ones.

Figure 11a shows the schematic representation of the cell study on the implants. Figure 11b shows the cell viability, which was determined on the basis of the live/dead cell assay. From the results, it was observed that the percentage of viable cells after 20 min of plasma exposure was 82% for treated GUR and 56% for treated Ti, whereas it was significantly lower for the control ranging from 24% to 27% in control GUR and control Ti, respectively. One tailed, paired student's t test analysis between the plasma treated groups revealed a strong statistical significance with $p < 0.01$. These results can be corroborated from the physicochemical results mentioned in the Characterization section, showing that plasma treatment creates a hydrophilic layer and enhances the surface properties. Additionally, these results are in accordance with literature results, which support that plasma treated implants induce better cellular compatibility,[40,41] likely due to the antimicrobial NO_x generation produced by plasma treatment.[42,43] Figure 11c shows the representative cell images, where the actin filaments are stained green and the nucleus is stained blue. The gene expression data shown in Figure 11d further support that the cells were differentiated into osteogenic stem cells showing the presence of RUNX2, osteopontin, and osteonectin genes on days 14 and 21, respectively. RUNX2 and osteonectin were expressed in nearly same levels on days 14 and 21. Osteopontin on the other hand showed elevated gene expression with 4-fold higher gene expression on day 21 in comparison to that on day 14. One tailed, paired student's t test was performed on the data to evaluate the statistical significance.

In order to show the 3D stem cell integration, X-ray μCT scans were performed after 21 days of cell culture on the surfaces. Figure 12 shows the μCT scan results for the control and treated polymeric and metallic substrates. Three-dimensional (isometric view and side view) images as well as top surface images showed better osteogenic stem cell integration to GUR and Ti6Al4V surfaces after plasma treatment compared to untreated control surfaces. Moreover, it can be seen that plasma treated implants are covered with both a monolayer and multilayer of cells. The control untreated surfaces showed substantially less stem cell coverage compared to treated ones. The 3D images of the top and cross-sectional constructs were in accordance with the fluorescence cell image results supporting the hypothesis of improved performance with plasma treatment.

4. CONCLUSIONS

The effect of a novel nonthermal plasma coating (PDD) generated by a handheld device was investigated on GUR1020 and Ti6Al4V sample surfaces by utilizing contact angle measurements, microhardness, ATR-FTIR, Raman spectrosco-

DOI: 10.1021/acsbiomaterials.9b00009
ACS Biomater. Sci. Eng. XXXX, XXX, XXX−XXX

py, XPS, XRD, tribological studies, corrosion studies, and biocompatibility examination. The results showed that the hydrophilicity of both polymeric and metallic substrates increased after the plasma exposure. The formation of new oxygen species as well as an increase in crystallinity of the polymer was confirmed by FTIR and Raman spectroscopy. Furthermore, it was observed that formation of a thin oxide layer on top of Ti6Al4V enhances the wear properties, corrosion behavior, and biocompatibility of the samples. From tribological assessments, the wear volume rate ratio was improved by approximately 60× after 20 min of plasma treatment in Ti6Al4V and GUR1020 samples. According to biocompatibility results, the plasma treated surfaces showed better osteogenic stem cell integration as confirmed by cell viability, fluorescence, and μCT imaging experiments.

■ ASSOCIATED CONTENT

Supporting Information

The Supporting Information is available free of charge on the ACS Publications website at DOI: 10.1021/acsbiomaterials.9b00009.

Chemical structure of GUR1020, experimental setup for the tribological experiment, schematic of osteogenic stem cell study timeline, 3D SRIM simulation, wear volume rate and wear volume rate ratio at different exposure times, statistical analysis of corrosion tests, and image analysis of stem cell grown on test pieces (Alizarin red S staining and μCT images) (PDF)

■ AUTHOR INFORMATION

Corresponding Author

*E-mail: mgartia@lsu.edu. Phone: +1-225-578-5900.

ORCID

Ardalan Chaichi: 0000-0002-0000-3637

Manas Ranjan Gartia: 0000-0001-6243-6780

Author Contributions

‖A.P. and L.K. contributed equally.

Notes

The authors declare no competing financial interest.

■ ACKNOWLEDGMENTS

The authors acknowledge the assistance of the Center for Advanced Microstructures and Devices (CAMD) staff at Louisiana State University for ATR-FTIR experiments and analysis. M.R.G. acknowledges the LSU start-up fund and Louisiana Board of Regents Support Fund (RCS Award Contract Number LEQSF(2017-20)-RD-A-04). A.C. is supported by LSU Economic Development Assistantships (EDA). A.P. is supported by the National Science Foundation (NSF Award Number 1660233). Raman, XPS, and XRD experiments were performed at LSU's Shared Instrumentation Facility (SIF). μCT imaging was conducted at the Louisiana School of Veterinary Medicine Micro-Computed Tomography Laboratory, funded through a Departmental Enhancement Program from the Louisiana Board of Regents Support Fund (BoRSF). The tribological testing was performed at LSU Center for Rotating Machinery (CeROM) laboratories. The fellowship for pursuing the postdoctorate training of L.K. at Louisiana State University, Louisiana, USA, hosted by M.M.K., was jointly provided by Indo-US Science and Technology Forum (IUSSTF) and the Science and Engineering Research Board (SERB), India.

■ REFERENCES

(1) Kunčická, L.; Kocich, R.; Lowe, T. C. Advances in metals and alloys for joint replacement. *Prog. Mater. Sci.* **2017**, *88*, 232−280.

(2) Clary, C.; Maletsky, L. Mechanical testing of knee implants. In *Mechanical Testing of Orthopaedic Implants*; Elsevier, 2017; pp 207−229.

(3) Carr, B. C.; Goswami, T. Knee implants−Review of models and biomechanics. *Mater. Eng.* **2009**, *30* (2), 398−413.

(4) Sharkey, P. F.; Hozack, W. J.; Rothman, R. H.; Shastri, S.; Jacoby, S. M. Why are total knee arthroplasties failing today? *Clin. Orthop. Relat. Res.* **2002**, *404*, 7−13.

(5) McEwen, H.; Barnett, P.; Bell, C.; Farrar, R.; Auger, D.; Stone, M.; Fisher, J. The influence of design, materials and kinematics on the in vitro wear of total knee replacements. *J. Biomech.* **2005**, *38* (2), 357−365.

(6) LaCour, M.; Komistek, R.; Meccia, B.; Sharma, A. In Forward Solution Model: Future Method for Predicting Knee and Hip Implant Longevity. *Orthopaedic Proceedings*; The British Editorial Society of Bone & Joint Surgery, 2016; pp 119−119.

(7) Raphel, J.; Holodniy, M.; Goodman, S. B.; Heilshorn, S. C. Multifunctional coatings to simultaneously promote osseointegration and prevent infection of orthopaedic implants. *Biomaterials* **2016**, *84*, 301−314.

(8) Kulkarni, M.; Mazare, A.; Schmuki, P.; Iglič, A. Biomaterial surface modification of titanium and titanium alloys for medical applications. *Nanomedicine* **2014**, *111*, 111.

(9) John, A. A.; Jaganathan, S. K.; Supriyanto, E.; Manikandan, A. Surface modification of titanium and its alloys for the enhancement of osseointegration in orthopaedics. *Curr. Sci.* **2016**, *111* (6), 1003.

(10) Wu, G.; Li, P.; Feng, H.; Zhang, X.; Chu, P. K. Engineering and functionalization of biomaterials via surface modification. *J. Mater. Chem. B* **2015**, *3* (10), 2024−2042.

(11) Kostov, K. G.; Nishime, T. M. C.; Castro, A. H. R.; Toth, A.; Hein, L. R. d. O. Surface modification of polymeric materials by cold atmospheric plasma jet. *Appl. Surf. Sci.* **2014**, *314*, 367−375.

(12) Guo, J.; Huang, K.; Wang, J. Bactericidal effect of various non-thermal plasma agents and the influence of experimental conditions in microbial inactivation: A review. *Food Control* **2015**, *50*, 482−490.

(13) Lunov, O.; Zablotskii, V.; Churpita, O.; Jäger, A.; Polívka, L.; Syková, E.; Dejneka, A.; Kubinová, Š. The interplay between biological and physical scenarios of bacterial death induced by non-thermal plasma. *Biomaterials* **2016**, *82*, 71−83.

(14) Regula, C.; Ihde, J.; Stepanov, S. Atmospheric Pressure Plasma Jets for Surface Activation Prior to Bonding and Painting. *Shikizai Kyokaishi* **2017**, *90* (8), 282−287.

(15) Wang, R.; He, X.; Gao, Y.; Zhang, X.; Yao, X.; Tang, B. Antimicrobial property, cytocompatibility and corrosion resistance of Zn-doped ZrO2/TiO2 coatings on Ti6Al4V implants. *Mater. Sci. Eng., C* **2017**, *75*, 7−15.

(16) Ataee, A.; Li, Y.; Fraser, D.; Song, G.; Wen, C. Anisotropic Ti-6Al-4V gyroid scaffolds manufactured by electron beam melting (EBM) for bone implant applications. *Mater. Des.* **2018**, *137*, 345−354.

(17) Yadroitsev, I.; Krakhmalev, P.; Yadroitsava, I. Selective laser melting of Ti6Al4V alloy for biomedical applications: Temperature monitoring and microstructural evolution. *J. Alloys Compd.* **2014**, *583*, 404−409.

(18) Wang, K.; Xiong, D.; Deng, Y.; Niu, Y. Ultra-lubricated surface of Ti6Al4V fabricated with combination of porous TiO2 layer, ultra-high molecular weight polyethylene film and hydrophilic polymer brushes. *Mater. Des.* **2017**, *114*, 18−24.

(19) Ren, J.; Liu, X.-B.; Lu, X.-L.; Yu, P.-C.; Zhu, G.-X.; Chen, Y.; Xu, D. Microstructure and tribological properties of self-lubricating antiwear composite coating on Ti6Al4V alloy. *Surf. Eng.* **2017**, *33* (1), 20−26.

DOI: 10.1021/acsbiomaterials.9b00009
ACS Biomater. Sci. Eng. XXXX, XXX, XXX−XXX

(20) Chandramohan, P.; Bhero, S.; Obadele, B. A.; Olubambi, P. A. Laser additive manufactured Ti−6Al−4V alloy: tribology and corrosion studies. *Int. J. Adv. Manuf. Technol.* **2017**, *92* (5−8), 3051−3061.
(21) Gallardo-Moreno, A. M.; Pacha-Olivenza, M. A.; Saldaña, L.; Pérez-Giraldo, C.; Bruque, J. M.; Vilaboa, N.; González-Martín, M. L. In vitro biocompatibility and bacterial adhesion of physico-chemically modified Ti6Al4V surface by means of UV irradiation. *Acta Biomater.* **2009**, *5* (1), 181−192.
(22) Hunt, B. J.; Joyce, T. J. A tribological assessment of ultra high molecular weight polyethylene types GUR 1020 and GUR 1050 for orthopedic applications. *Lubricants* **2016**, *4* (3), 25.
(23) Enqvist, E.; Ramanenka, D.; Marques, P. A.; Gracio, J.; Emami, N. The effect of ball milling time and rotational speed on ultra high molecular weight polyethylene reinforced with multiwalled carbon nanotubes. *Polym. Compos.* **2016**, *37* (4), 1128−1136.
(24) Sobieraj, M.; Rimnac, C. Ultra high molecular weight polyethylene: mechanics, morphology, and clinical behavior. *J. Mech. Behav. Biomed. Mater.* **2009**, *2* (5), 433−443.
(25) Mimaroglu, A.; Unal, H. Investigation of the water lubricated tribological behavior of medical grade UHMWPE. *Adv. Mater. Process. Technol.* **2015**, *1* (1−2), 109−114.
(26) Utzschneider, S.; Harrasser, N.; Schroeder, C.; Mazoochian, F.; Jansson, V. Wear of contemporary total knee replacements−a knee simulator study of six current designs. *Clin. Biomech.* **2009**, *24* (7), 583−588.
(27) Musib, M. K. A review of the history and role of UHMWPE as a component in total joint replacements. *Int. J. Biol. Eng.* **2011**, *1* (1), 6−10.
(28) Cho, E. H.; Lee, S. G.; Kim, J. K. Surface modification of UHMWPE with γ-ray radiation for improving interfacial bonding strength with bone cement (II). *Curr. Appl. Phys.* **2005**, *5* (5), 475−479.
(29) Visco, A.; Torrisi, L.; Campo, N.; Picciotto, A. Comparison of surface modifications induced by ion implantation in UHMWPE. *Int. J. Polym. Anal. Charact.* **2010**, *15* (2), 73−86.
(30) Gilman, A.; Piskarev, M.; Kuznetsov, A.; Ozerin, A. Modification of ultrahigh-molecular-weight polyethylene by low-temperature plasma. *High Energy Chem.* **2017**, *51* (2), 136−144.
(31) Kalin, M.; Vižintin, J. Use of equations for wear volume determination in fretting experiments. *Wear* **2000**, *237* (1), 39−48.
(32) Molinari, A.; Straffelini, G.; Tesi, B.; Bacci, T. Dry sliding wear mechanisms of the Ti6Al4V alloy. *Wear* **1997**, *208* (1−2), 105−112.
(33) Li, J.; Zanata, F.; Curley, J. L.; Martin, E. C.; Wu, X.; Dietrich, M.; Devireddy, R. V.; Wade, J. W.; Gimble, J. M.; Shah, F. S. The relative functionality of freshly isolated and cryopreserved human adipose-derived stromal/stem cells. *Cells Tissues Organs* **2016**, *201* (6), 436−444.
(34) Shaik, S.; Wu, X.; Gimble, J.; Devireddy, R. Effects of decade long freezing storage on adipose derived stem cells functionality. *Sci. Rep.* **2018**, *8* (1), 8162.
(35) Livak, K. J.; Schmittgen, T. D. Analysis of relative gene expression data using real-time quantitative PCR and the 2− ΔΔCT method. *Methods* **2001**, *25* (4), 402−408.
(36) Durdu, S.; Usta, M.; Berkem, A. S. Bioactive coatings on Ti6Al4V alloy formed by plasma electrolytic oxidation. *Surf. Coat. Technol.* **2016**, *301*, 85−93.
(37) Fazel, M.; Salimijazi, H.; Golozar, M.; Garsivaz Jazi, M. R. A comparison of corrosion, tribocorrosion and electrochemical impedance properties of pure Ti and Ti6Al4V alloy treated by micro-arc oxidation process. *Appl. Surf. Sci.* **2015**, *324*, 751−756.
(38) Vaithilingam, J.; Goodridge, R. D.; Hague, R. J.; Christie, S. D.; Edmondson, S. The effect of laser remelting on the surface chemistry of Ti6al4V components fabricated by selective laser melting. *J. Mater. Process. Technol.* **2016**, *232*, 1−8.
(39) Kar, S.; Molla, M. S.; Katti, D. R.; Katti, K. S. Tissue-engineered nanoclay-based 3D in vitro breast cancer model for studying breast cancer metastasis to bone. *J. Tissue Eng. Regener. Med.* **2019**, *13* (2), 119−130.
(40) Somayajula, D. A. *Biocompatibility of Osteoblast Cells on Titanium Implants*; Cleveland State University, 2008.
(41) Kubinova, S.; Zaviskova, K.; Uherkova, L.; Zablotskii, V.; Churpita, O.; Lunov, O.; Dejneka, A. Non-thermal air plasma promotes the healing of acute skin wounds in rats. *Sci. Rep.* **2017**, *7*, 45183.
(42) Pavlovich, M.; Ono, T.; Galleher, C.; Curtis, B.; Clark, D.; Machala, Z.; Graves, D. Air spark-like plasma source for antimicrobial NOx generation. *J. Phys. D: Appl. Phys.* **2014**, *47* (50), 505202.
(43) Xu, Z.; Shen, J.; Cheng, C.; Hu, S.; Lan, Y.; Chu, P. K. In vitro antimicrobial effects and mechanism of atmospheric-pressure He/O2 plasma jet on Staphylococcus aureus biofilm. *J. Phys. D: Appl. Phys.* **2017**, *50* (10), 105201.

DOI: 10.1021/acsbiomaterials.9b00009
ACS Biomater. Sci. Eng. XXXX, XXX, XXX−XXX